

*CHAPTER 4*  
*ELECTRO-OPTIC PROPERTIES*  
*OF*  
*GALLIUM Pnictide*  
*HETEROSTRUCTURE NANOWIRES*

## 4.1 Introduction

Since the invention of nanostructure domain, the material design, development and fabrication techniques have evolved exponentially with ultra-fast rates.<sup>1</sup> The three distinct types of nanostructures namely, 0D, 1D and 2D nanomaterials possess dimension and confinement dependent unique transport and dynamical properties.<sup>2</sup> Much more efficiency can be attained by modulating the carrier dynamics within the material; which is done by varying chemical composition of the nanostructures,<sup>3</sup> or by applying external strain/pressure,<sup>4</sup> or by creating defects.<sup>5,6</sup> The aforementioned pathways have been successfully utilized for fabricating optoelectronic and nanoelectronic devices;<sup>7-11</sup> but in case of materials to be utilized for energy applications like photovoltaics and water-splitter catalyst materials, it is necessary to ensure the separation of charge carriers in distinct layers within the nanomaterial so that the overall efficiency can be enhanced.<sup>12</sup> Here comes the role of heterostructured geometry, that not only helps to trap the charge carriers within different regions but also provides an opportunity to tune the properties of a nanomaterial for multifunctional applications.<sup>13-15</sup> The heterostructure (HS) may consist two or more materials embedded on each other vertically/horizontally/radially/axially depending on the dimensional confinement and respective application. Formation of HS can be done easily and feasibly if the constituent materials possess least minimum lattice mismatch; this is necessary for successful growth of HS, as large lattice mismatch between the heterolayers induces strain within the system that cause reduction in stability.<sup>16</sup> Comparing three distinct kinds of nanomaterials, the formation of 1D HSs have been recognized as an efficient method due to its ability to

release strain in radial directions, thereby making the growth of 1D HSs with large lattice mismatch between constituent materials possible.<sup>17-21</sup> As far as 1D-1D HSs are concerned, there are two possible configurations: radial and axial. The radial 1D HSs are formed when one of the 1D nanomaterial is surrounded by other 1D nanomaterial(s), so as to form core-shell like geometry; while the 1D axial HSs can be made by growing different 1D nanomaterials on each other along a fixed growth direction with same or different stacking configurations.<sup>19,21-23</sup> Apart from the plethora of research activities dedicated to the distinct types of nanostructures, the two-dimensionally confined one-dimensional (1D) nanostructures like nanotubes (NTs), nanoribbons (NRs) and nanowires (NWs) have grabbed the paramount importance owing to their versatile properties like strong quantum confinement,<sup>2</sup> carrier trapping<sup>24,25</sup> and moderate electronic bandgaps.<sup>26,27</sup> Plenty of research articles explaining the growth mechanism,<sup>28</sup> phase engineering<sup>29,30</sup> and heterostructuring<sup>31,32</sup> of the NWs render the significance of these 1D systems owing to their versatile nature and multiple applicability. Further, these 1D systems when especially constructed by combining the group III and V elements, yield tremendously unexpected results.<sup>33</sup> One can also find vast documentation on the dramatic behaviour of the III-V NWs subjected to heterostructuring.<sup>34,35</sup> As the spatial electronic states of the material(s) which are already modified through imposition of two-dimensional confinement, are still subjected to finer modulation under heterostructured configuration. This technique has been utilized widely to achieve desired transport through the system qualitatively and quantitatively.<sup>36-39</sup> As it has been usually observed, introducing heterostructured geometry causes lattice mismatch between the heterolayers due to

the difference in their structural parameters under pristine conditions. This could be one of the factors responsible for trapping the charge carriers or for elongating the carrier recombination rates,<sup>17,18,40</sup> that further helps to understand the transport mechanism taking place at the hetero-interface. Further, for obtaining desired properties with feasible stability, it is expected that the lattice mismatch between the constituent materials of the HS should be minimum or lie within acceptable range. The more mismatch, causes more strain generated in the system, although in case of one-dimensional heterostructure nanowires (1D HSNWs), the generated strain gets released in radial directions and thus, desired stability is achieved with unique interface properties.<sup>41</sup> Considering the practical conditions, the literature survey on III-V HSNWs for past few decades includes successful synthesis of radial and axial HSNWs by employing VLS method which not only facilitates the growth of the HSNWs with distinct lattice constants of shell and core materials but also for the materials that possess significantly large lattice mismatch with the substrate material.<sup>19-22</sup> The prime reason for the same is the release of strain through the free surface of the NWs via radial direction.<sup>42,43</sup> One of the studies on GaAsP/GaP core/shell NW by Himwas et al. shows unintentional occurrence of core/shell geometry on deviating the As and P content in GaAsP NW.<sup>23,44</sup> Furthermore, the authors observed that these NWs without passivation does not show markable luminescence properties; however, on passivating the NW with GaP shell induces extra peak in PL spectra confirming optical transition. Combining the III-V HSNWs with V material shell is reported by Zhang et al.<sup>45,46</sup> which suggests strong carrier confinement owing to large differences in the bandgap of AlGaIn shell layer.

In addition to their capacity as 1D NW devices, semiconductor NWs are excellent nanostructured materials for exploring physics in reduced dimensions and in complex geometries. Quian et al. reported the growth and characterization of core/multishell (CMS) n-GaN/  $\text{In}_x\text{Ga}_{1-x}\text{N}$ /GaN/p-AlGaN/p-GaN radial HSNWs that exhibit well-defined and reliable electrical n-type cores and p-type shells that behave as p-n diodes offering great promises as compact, efficient, reliable building blocks for integrated nanoscale photonic systems, including multicolor LEDs and lasers.<sup>47</sup> Recently, Wang et al. presented solvent-mediated, surface reaction-driven growth route for synthesis of CdS NW/CdIn<sub>2</sub>S<sub>4</sub> NS 1D/2D which exhibits much higher visible-light-responsive photocatalytic activities<sup>10</sup> whereas, the group of Li et al. fabricated a high-performance ultraviolet photodetectors based on a heterojunction device structure using ZnO quantum dots (QDs) decorated Zn<sub>2</sub>SnO<sub>4</sub> NWs and, it was shown that the novel configuration improved the device performance that can be utilized in flexible and wearable devices.<sup>48</sup> Zheng et al reported UV-vis-NIR sensitive ZnO NWs array/PbS QDs Hs<sup>49</sup> and Zhang et al. demonstrated highly selective and ultra-sensitive photodetection of UV-A rays using a bicrystalline GaN based NWs.<sup>9</sup> Plissard et al. reported gold-free axial and lateral GaAs/GaAsSb HSNWs on silicon for application in future solar cell designs.<sup>50</sup> Group III-As/III-Sb heterostructure NWs are of special interest due to their integration in high speed electronic devices or long-wavelength optical devices<sup>7,11</sup> along with their capability of presenting a fundamental platform for the study of basic physical principles in condensed matter such as Majorana fermions.<sup>51</sup>

In the present chapter, we have constructed the 1D HSNWs by combining the NWs made-up of III-V compounds like gallium phosphide (GaP), gallium arsenide (GaAs) and gallium antimonide (GaSb) for the investigation of the composition, shape and geometry dependent structural, electronic and optical properties of the GaSb-GaP and GaSb-GaAs HSNWs with core/shell geometry under Kohn-Sham formulated *first-principles* density functional theory (DFT)<sup>52</sup> approach. DFT being an *ab initio* tool, that treats the systems quantum mechanically has received vast acceptance throughout the globe on account of its accurate predictive power of ground state properties of conventional and newly emerging materials within bulk as well as nano regimes<sup>52</sup> and with extrapolated advancing trend of the initial approximation has further put forth this approach as the kingpin of the theories utilized for material property investigations.

## 4.2 Computational Details

The Kohn-Sham formulated DFT<sup>52</sup> is utilized for computing the structural, electronic and optoelectronic properties of the HSNWs with gallium antimonide (GaSb) as a core NW shielded with two distinct shells made up from gallium phosphide (GaP) and gallium arsenide (GaAs) NWs, respectively. For constructing the HSNWs, the pristine GaSb NW with Wurtzite (WZ) phase grown in 0001 direction was cut in respective directions for obtaining desired core morphologies with circular and triangular cross-sections respectively (see Fig. 4.1), and then were masked with the respective shells of GaP or GaAs NWs so as to achieve hexagonal cross-sectional geometry. The next step was to assess and saturate the unsatisfied valencies of the atoms present at the surface of the HSNWs that are responsible for the pseudo electronic states originating due to

surface dangling bonds. To remove the surface dangling bonds present in these bare HSNWs, the HSNWs were then passivated by adding required number of pseudo hydrogen adatoms on the HSNW surface atoms with unsatisfied valencies. These finally constructed HSNWs were then considered for optimization procedure that was done by self-consistently minimizing the total-energy of the systems with respect to HSNW shape, size and atomic positions under Broyden-Fletcher-Goldfarb-Shanno (BFGS) algorithm.<sup>53</sup> The local density approximated (LDA) pseudopotentials describing atomic orbitals in form of frozen cores and valence electrons with Perdew-Zunger parameterization scheme were incorporated for solving the many-body Kohn-Sham equation.<sup>54,55</sup> To address slight lattice mismatch between the core and shell of the HSNWs, and for accurate prediction of energetics of the HSNWs, the contributions from long range van der Waals forces were incorporated by applying dispersion correction to the exchange-correlation functionals.<sup>56</sup> The high kinetic energy cut-off of 816 eV for electronic wave-function was found sufficient for converging the total-energy and total stress/atom within the threshold criterions 0.00001 eV and 0.001 eV/atom, respectively. The integration of Brillouin Zone (BZ) along the high-symmetry points was performed with  $\Gamma$  centered MP scheme<sup>57</sup> based dense grids with weightage  $1 \times 1 \times 10$ . The atoms were masked by adding smearing of magnitude 0.07 eV with Marzari-Vanderbilt function.<sup>58</sup> The electronic transport mechanism was assessed by computing the electronic band structure of the HSNWs along high-symmetry path of the BZ in  $\Gamma$ -Z direction. The individual atomic orbitals contributing to overall transport of the HSNWs was decomposed and analysed by computing the partial electronic density of states (PDOS). After understanding the structural and

electronic properties, the optical transport is through the HSNWs is assessed by means of computing the frequency dependent complex di-electric function of the systems under random phase approximation (RPA).<sup>59,60</sup> Utilizing the imaginary and real parts of the complex di-electric function, and the Kramers-Kronig relation, further calculations were performed for evaluating optical properties like extinction coefficient, loss function, reflectivity, refractive index and finally, the absorption coefficient.<sup>61</sup> Apart from computation of the electro-optic properties of the HSNWs, the solar cell parameters of the systems are computed for investigating the solar power conversion efficiency of the systems. The parameters like open-circuit voltage ( $V_{OC}$ ), short-circuit current density ( $J_{SC}$ ), Fill Factor (FF) and efficiency ( $\eta$ ) were computed under Shockley-Queisser (SQ) limit. Theoretically, the  $J_{SC}$  is computed with the help of equation given below:<sup>62,63</sup>

$$J_{SC} = \int_0^{\infty} eA(E) I_{Sun}(E) dE \quad (4.1)$$

The  $I_{Sun}$  represent the solar flux density taken at AM1.5G spectrum and  $A(E)$  is the absorbance of the material which is computed using the formula,

$$A(E) = 1 - \exp^{-2\alpha L} \quad (4.2)$$

Here,  $L$  is the thickness of the material and the  $\alpha$  is the respective absorption coefficient. For reverse saturation current density,  $J_0$ , we have utilized the equation below:

$$J_0 = \int_0^{\infty} e\pi A(E) I_{bb}(E) dE \quad (4.3)$$

Here, the  $I_{bb}(E)$  being the black-body spectrum is considered with unit magnitude, and  $e$  is the electronic charge. This gives overall current density  $J$  as,

$$J = J_{SC} - J_0 \left( e^{\frac{eV}{kT}} - 1 \right) \quad (4.4)$$

Here, the symbols  $k$ ,  $T$  and  $V$  respectively present the Boltzmann constant, temperature (300 K) and potential generated over the absorber layer of the solar cell. Considering the above equations, we can obtain the maximum power  $P_{MAX}$  from the J-V curve computed under SQ approach and the corresponding solar power conversion efficiency can be evaluated.

$$\eta = \frac{P_{MAX}}{P_{IN}} \quad (4.5)$$

## 4.3 Results and Discussion

### 4.3.1 Structural Properties

The optimization of the crystal structure is of utmost importance as, the correct prediction of inter-atomic distances, angles and lattice constants are the raw materials for the computation of other ground state properties. Prior to the formation of the NW, and finally, the HSNWs, the LDA computed structural parameters of the GaX compounds under bulk configuration reasonably agree with reported data,<sup>64</sup> validating the approach. As far as heterostructured geometry is concerned, it is preferable that the hetero-layers or hetero-materials possess minimum lattice mismatch, as large mismatch may lead to less stable configuration with imperfect crystal structure. Lattice matched materials ensure the elimination of intrinsic strain generated at the hetero-interface and provide structural stability thereby making the

growth of the HS possible under practical conditions. Keeping this in mind, the sibling NWs from gallium pnictide family have been selected for the construction of the HSNWS. The three NWs, GaP, GaAs and GaSb with hexagonal cross-sections were

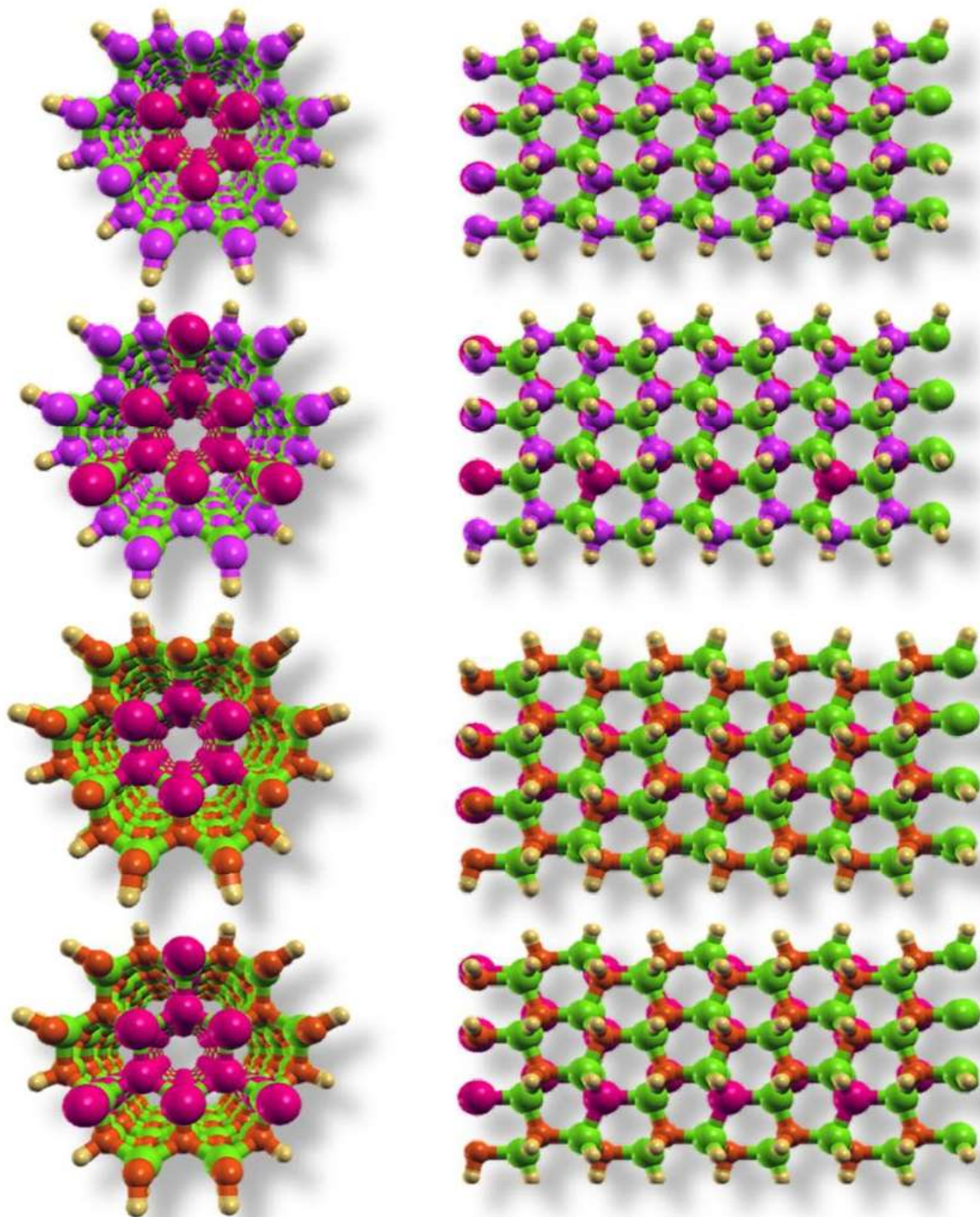


Figure 4.1. Top and Side views of optimized crystal structures of GaSb-GaAs and GaSb-GaP HSNWs with round (R) and triangular (T) cores, respectively. The atoms in Green, Pink, Purple, Orange and Yellow represent the atoms of Ga, Sb, As, P and H, respectively.

considered for constructing core/shell like geometry; a radial HSNW. To assess the shape dependent properties, two distinct shapes, i.e. triangular and circular (see **Computational Details**) NWs were considered for core NW, keeping the overall cross-section of the HSNW hexagonal (see Fig. 4.1). The GaSb NW in all cases was fixed as a core NW, with GaP and GaAs NWs varied as the shell NW respectively, making total four configurations of the HSNWs. The well-optimized structural geometries of the HSNWs as presented in Figure 4.1 show slight modification in the cross-sectional geometry as compared to the pristine NWs (see **CHAPTER 3**) which is attributed to the replacement of the heavier Sb atoms with the lighter P/As atoms forming the shell NW. The optimized structural parameters with corresponding electronic parameters are listed in Table 4.1. As it can be observed from the Table 4.1, the lattice parameters of the four HSNWs, fall within the range of corresponding pristine NWs. It is noteworthy that despite of significant lattice mismatch of the GaAs/GaP NWs with the reference NW GaSb, the formation of the HSNW is quite favourable due to its ability of compensating the generated strain in radial directions. One of the ways of estimating the structural stability of any system is to compute its cohesive energy (see Equation 4.6).

$$E_{Coh}^{HSNW} = \left( \frac{(n_{Ga}\mu_{Ga} + n_{Sb}\mu_{Sb} + n_X\mu_X + n_H\mu_H) - (E_{Total}^{HSNW})}{N} \right) \quad (4.6)$$

Here, the terms  $\mu$  and  $n$  represent the chemical potential and respective number of atoms of corresponding atomic species with  $N$  being the total number of atoms in the HSNW (symbol  $X$  represent As, P for GaSb-GaP and GaSb-GaAs HSNW,

respectively). The computed magnitudes of cohesive energy per atom (see Table 4.1) reveal that the HSNWs with both configurations (R and T cores) possess higher cohesion as compared to the pristine NWs; this implicates that the formation of HSNW is favourable with selected configurations. Surprisingly, despite of significant mismatch between the in-plane lattice constants of the GaP and GaSb NWs, the energy of cohesion is found more pronounced than the GaAs counterpart. It is interesting to note that the spatial lattice alignment of the hetero-materials may lead to dramatic modulation in the electronic properties; this feature plays crucial role in band-edge alignments of the constituent hetero-layers and provides an opportunity for carving desired type of hetero-interface.

**Table 4.1.** Computed structural and electronic parameters of GaSb-GaAs and GaSb-GaP HSNWs together with pristine GaP, GaAs and GaSb NWs.

System	Shape of core NW	Lattice Parameter (Å)	Cohesive Energy (eV/atom)	VBM (eV)	CBM (eV)	E <sub>g</sub> (eV)
<b>GaSb</b>	-	6.973	3.782	-2.684	-0.996	1.68
<b>GaSb-GaAs</b>	Round (R)	6.482	7.658	-2.360	-0.528	1.83
	Triangular (T)	6.560	5.925	-2.329	-0.489	1.84
<b>GaAs</b>	-	6.429	4.175	-2.925	-0.647	2.27
<b>GaSb</b>	-	6.973	3.782	-2.684	-0.996	1.68
<b>GaSb-GaP</b>	Round (R)	6.327	8.908	-2.417	-0.513	1.90
	Triangular (T)	6.456	6.626	-2.531	-0.621	1.91
<b>GaP</b>	-	6.197	4.494	-1.491	1.093	2.58

### 4.3.2 Electronic Properties

Apart from the first condition for formation of HS, i.e. the reduced lattice mismatch, the second key to unlock the desired transport through the HS is to align the electronic

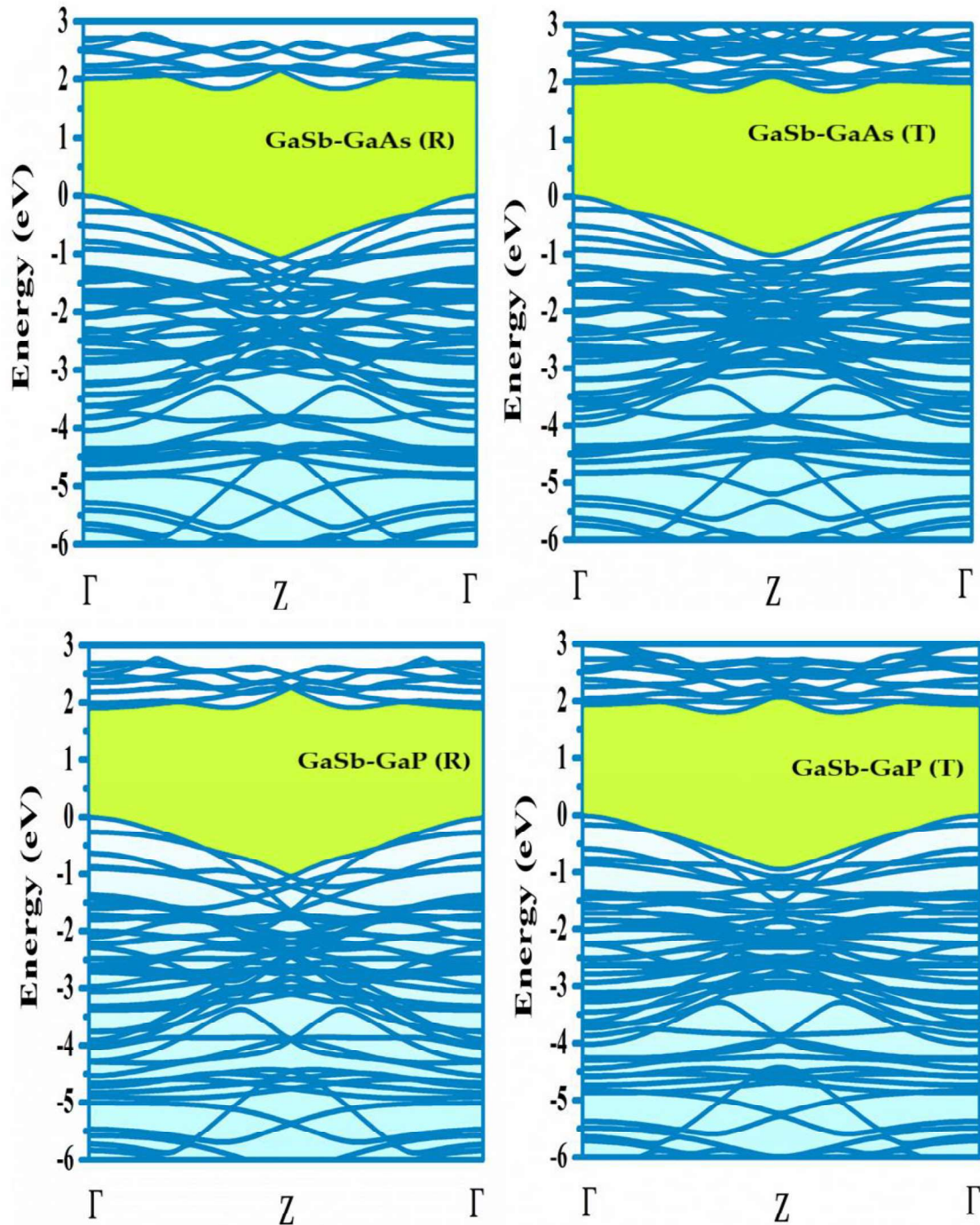


Figure 4.2. Computed electronic band structures of GaSb-GaAs and GaSb-GaP HSNWs with round (R) and triangular (T) cores, respectively.

edge states apparently so as to achieve desirable type of HS. The efficient optoelectronic and photovoltaic devices require specific separation of the charge carriers that solely depends on the type of HS, and out of all HS alignments, the type-II HS stands out as a desirable candidate due to its prolonged carrier life-times and recombination rates. To deeply investigate the electronic band edge alignments of the HSNWs, the electronic band structures and partial density of states (PDOS) are computed and presented in Figures 4.2 and 4.3, respectively. To get insight to the actual band-edge alignment of these HSNWs, the core and shell NWs of the respective HSNWs were individually optimized and corresponding electronic band structures were computed (see Figs. 4.4 and 4.5 for GaSb-GaAs and GaSb-GaP HSNWs, respectively). Also, to have a comparative assessment of the HSNWs with their constituent materials under bulk and NW configurations, we have plotted the edge states (not exactly to the scale) and presented in Figure 4.6. As it can be viewed from the Figure 4.2, the electronic band structures show indirect nature for all HSNWs, except for GaSb-GaP (R) HSNW which shows direct nature, in contrast to its bulk and NW pristine configurations.<sup>64</sup> Comparing the gap magnitudes of the HSNWs with bulk and NW configurations, it is obvious to predict higher bandgap than the bulk phase due to quantum confinement effects, yet it is important to understand the modifications in these effects on introduction of heterostructured geometry.

As it can be observed (see Table 4.1), the HSNWs possess intermediate bandgap between the constituent pristine NWs. Introducing GaAs/GaP as the shell NW increases in bandgap indicating enhancement in the semiconducting properties of the HSNWs. Also, the T-core configuration in both cases possess higher bandgap than the

R-core configured HSNW, unravelling special role of geometry and composition on the electronic transport properties. Also, the GaSb-GaX (X=As, P) HSNWs for T-core possess higher gap despite of enhancement in the metallic Sb content in both cases (see Table 4.1). The computed PDOS plots (see Fig. 4.3) reveal dramatic manipulation

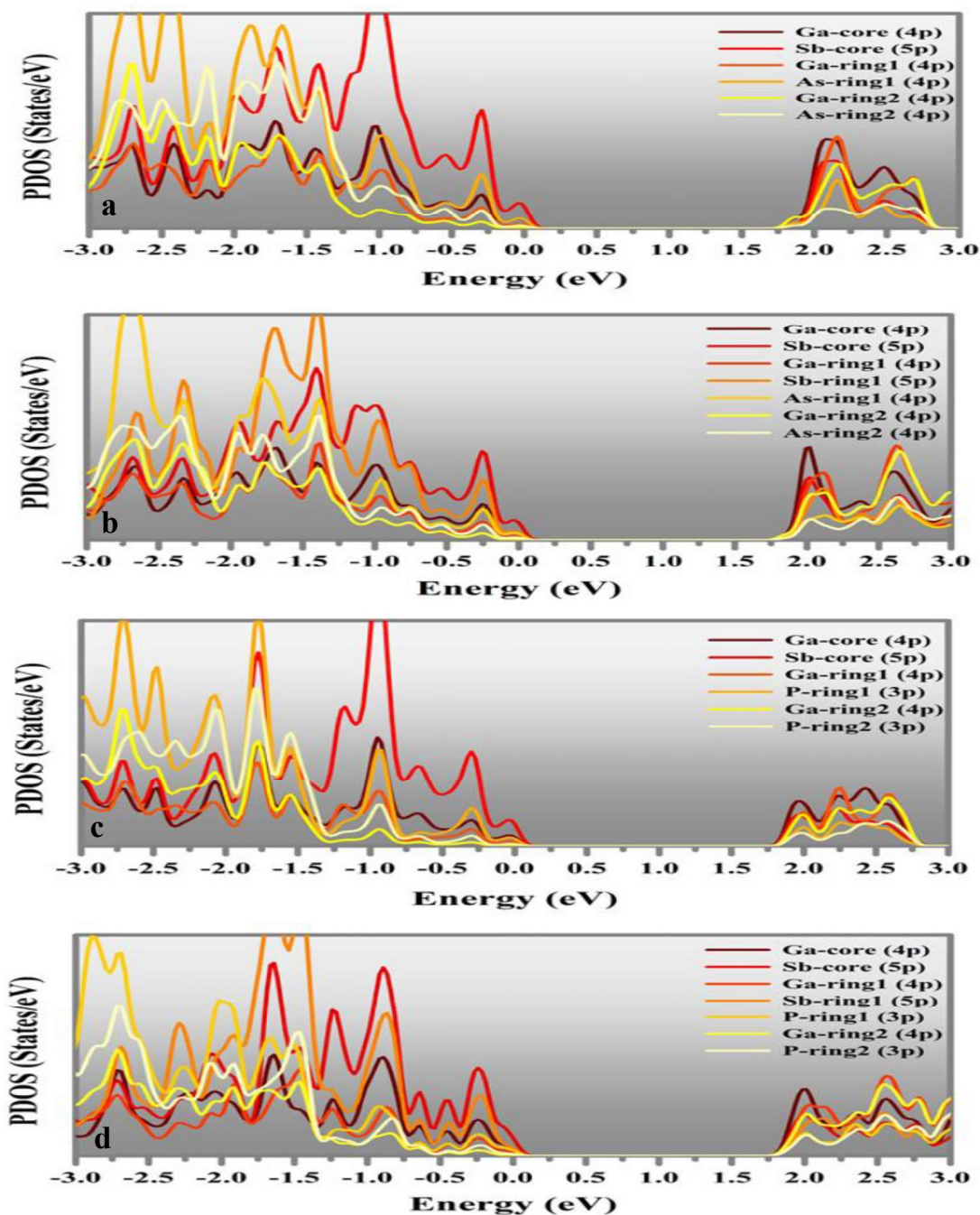


Figure 4.3. Computed partial electronic density of states (PDOS) of GaSb-GaAs (a, b) and GaSb-GaP (c, d) HSNWs with round (R) and triangular (T) cores, respectively.

of electronic contributions of individual atoms subjected to their position in the core or shell NW. Further, the atoms of same species but aligned at inner or outer edge of the core/shell NW behave apparently. For instance, all atomic species replicate markable contribution in the valence band regime, however, the valence band maxima (VBM) in all cases is highly populated by the Sb electrons. In case of conduction band regime (CBM), almost all species contribute to similar extent, yet the Ga electrons

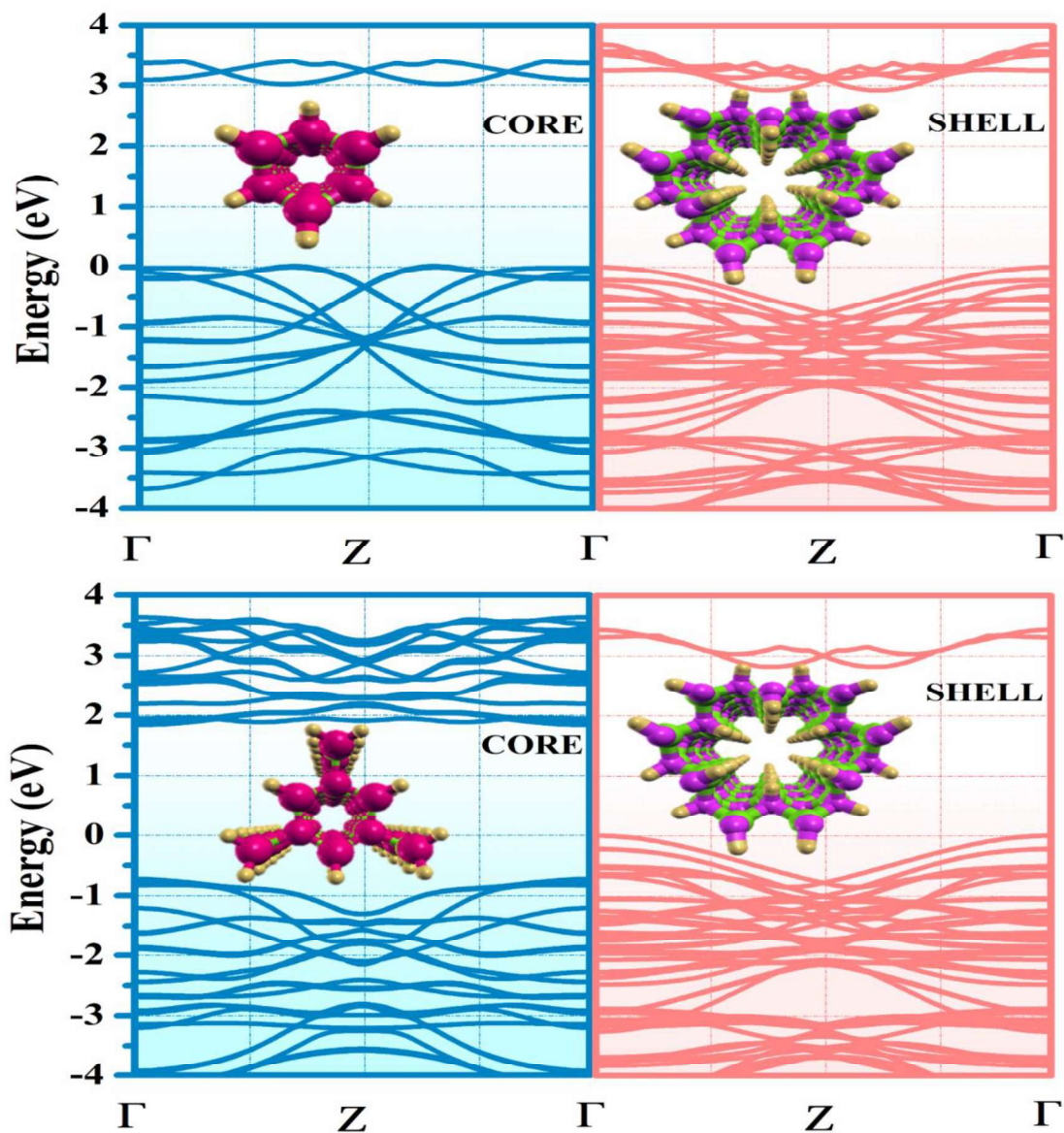


Figure 4.4. Computed electronic band structures of individual core and shell NWs of GaSb-GaAs HSNW with round (upper panel) and triangular (lower panel) cores, respectively.

possess dominance over other atoms by virtue of their significant population near the CBM edge states (see Fig. 4.3).

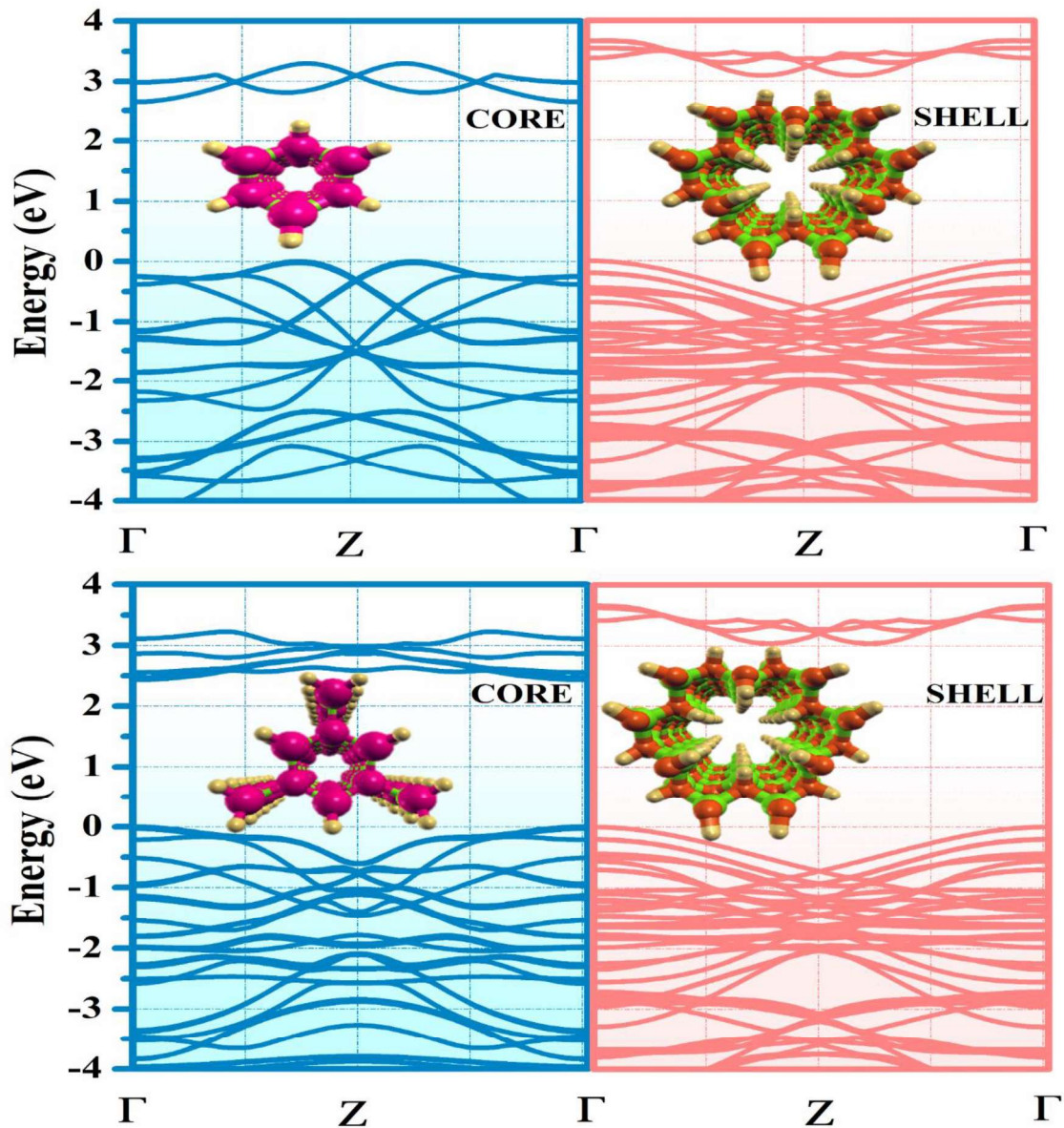


Figure 4.5. Computed electronic band structures of individual core and shell NWs of GaSb-GaAs HSNW with round (upper panel) and triangular (lower panel) cores, respectively.

Now, after understanding the electronic transport through the overall HSNWs, it is important to investigate the role of core and shell NWs individually to understand the band alignment between the heterolayers of the NWs. To understand this, the R and T core NWs made up of GaSb NW and, the respective GaAs/GaP shell NWs were

systematically investigated to unravel their role in electronic transport (see Figs. 4.4 & 4.5). The computed independent electronic band structures of the core and shell NWs of GaSb-GaAs (see Fig. 4.4) for R and T-shaped core clearly indicates that the electronic nature of the core NW is found direct in both cases, while it is indirect for corresponding shell NWs. Similar observations are obtained for GaSb-GaP HSNWs (see Fig. 4.5), in which the T-core GaSb-GaP HSNW follows same trend as the GaSb-GaAs HSNWs, whereas, the R-core HSNW possess indirect bandgap in case of both core and shell NWs (see Fig. 4.5).

Talking about the spatial type of band alignment, the computed edge states (not to the scale) of the core and shell NWs are plotted draw a clear picture of size, shape and

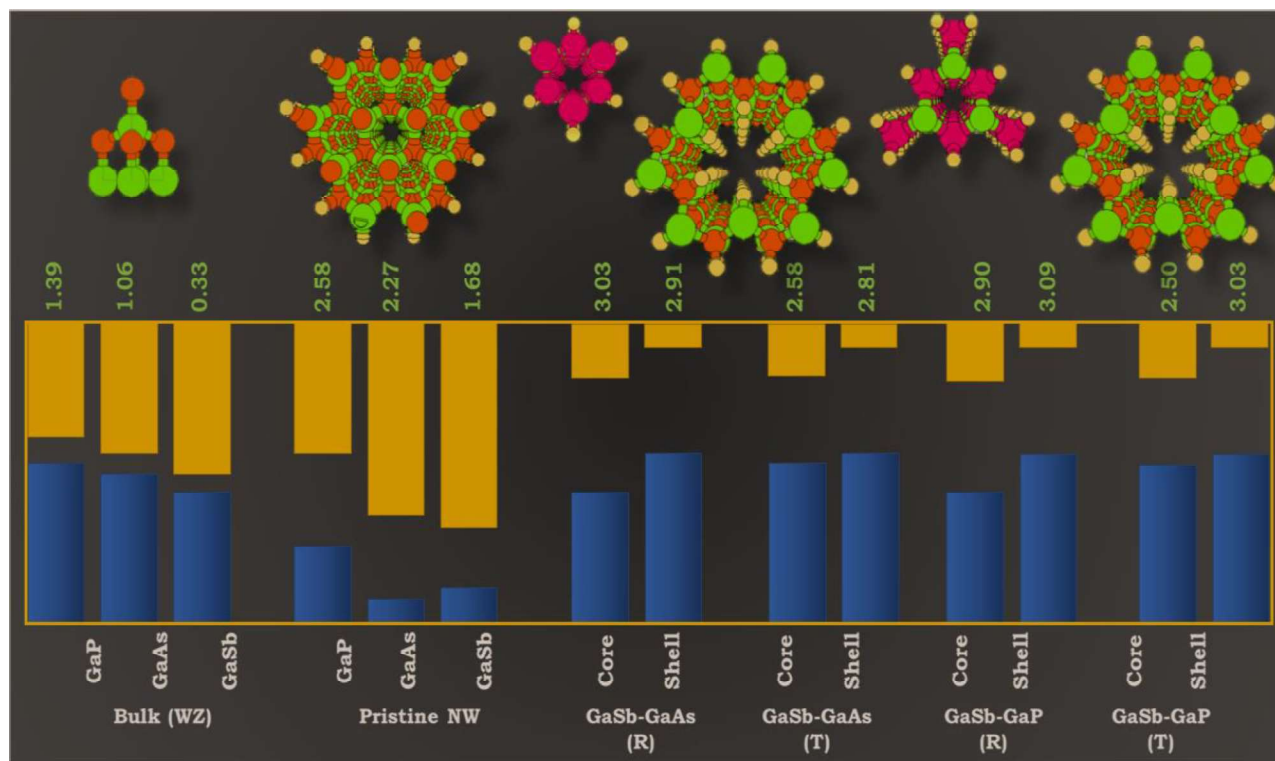


Figure 4.6. Schematic representation of band edge alignments (not to the scale) of GaX (P, As, Sb) in bulk and NW forms and for core and shell NWs of corresponding HSNWs with GaSb NW as a shell NW (The schematic diagram on the top represent the crystal structures of the systems under bulk, NW and HSNWs dissected into core and shell structures with corresponding electronic band gaps in eV).

composition dependent modulation in the together with the bulk and NW configurations of GaX (X=P, As ,Sb) compounds to electronic edge states (see Fig. 4.7).

It can be clearly observed from the above figure, that on confining the GaX compounds significant expansion in the bandgap is achieved. Further, moving towards the core/shell band edge alignments, it is evident from the Figs. 4.4, 4.5 and 4.6, that the gap magnitude of the HSNWs lie within the optical regime of the electro-magnetic spectrum. Further, as desired, the edge alignment in all four HSNWs is of type-II; i.e. the VBM and CBM energies of the core NWs are lower than the corresponding VBM and CBM energies of the shell NWs with magnitudes lying within the optical spectrum makes these HSNWs most significant for the photovoltaic device applications. Furthermore, the spatially aligned band-edges together with the direct electronic nature in case of GaSb-GaP (R) HSNW validates its applicability in the opto-electronic devices also.

### **4.3.3 Optical Properties**

After understanding the electronic transport and band alignment properties of GaSb-GaX (X=As, P) HSNWs, the application of the HSNWs in the field of optoelectronics, the optical transport properties of the HSNWs were computed. The RPA<sup>59,60</sup> computed complex di-electric function as a function of photon frequency for all four HSNWs is presented in Fig. 4.7. The imaginary part of the complex di-electric function elucidates the absorption characteristics of the materials, and hence is of utmost important for revealing optical properties like refractive index, extinction co-efficient, reflectivity, etc. Utilizing Kramers-Kronig relations one can determine the real part of the complex di-electric function, that reveals key factors associated with non-linear optical

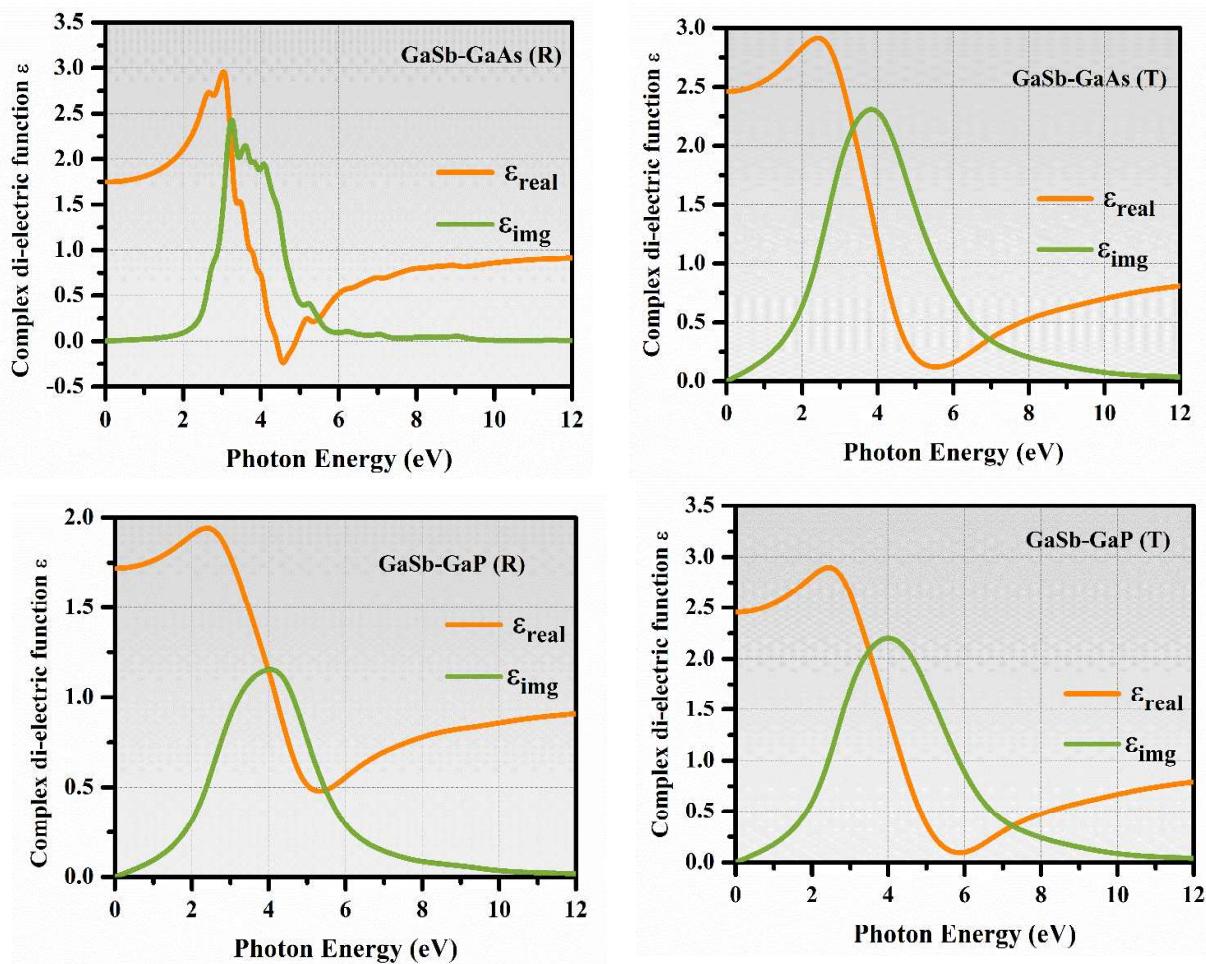


Figure 4.7. Computed real and imaginary components of complex di-electric function as a function of photon frequency for GaSb-GaAs and GaSb-GaP HSNWs for round (R) and triangular (T) cores, respectively.

phenomena like polarization. The relations of the complex di-electric function with remaining optical properties like refractive index, optical conductivity, etc., are discussed elsewhere (see CHAPTER 2). The computed absorption co-efficient of the GaSb-GaX (X=As, P) HSNWs spans a wide-spread area over the electro-magnetic spectral range even beyond optical regime (see Fig. 4.8); this makes these HSNWs significantly important for optoelectronic device applications. The observed trends of absorption co-efficient are consistent and resembles profiles of imaginary component of complex di-electric function (see Fig. 4.7).

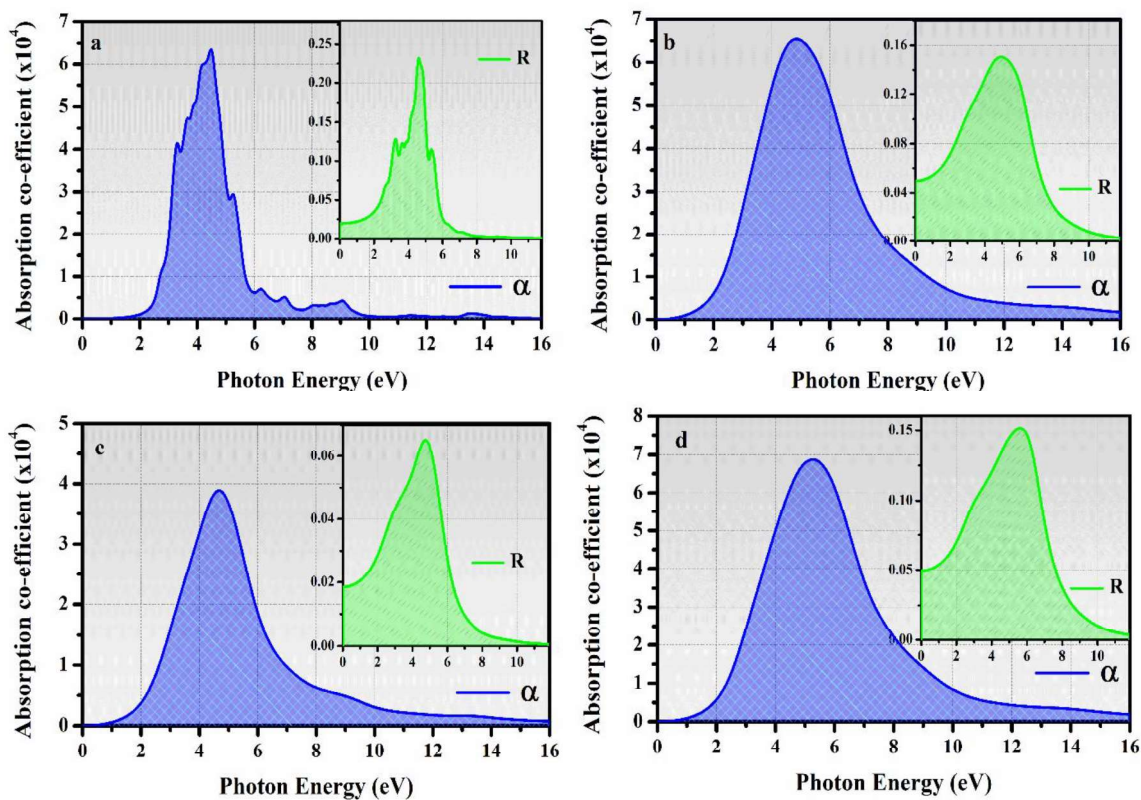


Figure 4.8. Computed absorption co-efficient of GaSb-GaAs (a, b) and GaSb-GaP (c, d) HSNWs with round (R) and triangular (T) core, respectively. The insets of the graphs represent reflectivity of corresponding system.

#### 4.3.4 Application to the Photovoltaic Solar Cells

Inspired from the electro-optic response of the GaX compounds under NW and HSNW configurations, we then computed the solar cell parameters of the systems for investigating their applicability to the photovoltaic (PV) devices. We have utilized the Shockley-Queisser (SQ) limit approach for assessing the overall power conversion efficiency of the GaX systems under NW and HSNW configurations. The Tables 4.2 and 4.3 respectively show the computed solar cell parameters of the GaX (X=P, As, Sb) NWs and GaSb-GaAs and GaSb-GaP HSNWs with round (R) and triangular (T) cores.

Table 4.2. Computed solar cell parameters for GaX (X=P, As, Sb) NWs under SQ limit.

parameters	Nanowires with diameter ~ 1, 2 and 3 nm								
	GaP1	GaP2	GaP3	GaAs1	GaAs2	GaAs3	GaSb1	GaSb2	GaSb3
<b>J (mA/cm<sup>2</sup>)</b>	5.26	11.855	16.814	9.318	17.757	25.290	23.023	37.55	40.34
<b>V<sub>oc</sub> (V)</b>	0.912	0.929	0.936	0.924	0.938	0.945	0.943	0.954	0.217
<b>FF (%)</b>	0.87	0.875	0.876	0.875	0.876	0.877	0.877	0.878	0.65
<b><math>\eta</math> (%)</b>	4.194	9.643	13.79	7.534	14.59	20.96	19.05	31.12	5.49

Table 4.3. Computed solar cell parameters of GaSb-GaAs and GaSb-GaP HSNWs together with their comparison to the pristine core and shell NWs.

System	Shape of core NW	E <sub>g</sub> (eV)	J (mA/cm <sup>2</sup> )	V <sub>oc</sub> (V)	FF (%)	$\eta$ (%)
GaSb NW	-	1.68	23.023	0.943	0.877	19.05
GaSb-GaAs HSNW	Round (R)	1.83	18.825	0.939	0.876	15.50
	Triangular (T)	1.84	18.519	0.939	0.876	15.24
GaAs NW	-	2.27	9.452	0.924	0.875	7.65
GaSb NW	-	1.68				
GaSb-GaP HSNW	Round (R)	1.90	16.968	0.937	0.876	13.93
	Triangular (T)	1.91	16.743	0.937	0.876	13.74
GaP NW	-	2.58	5.626	0.912	0.874	4.19

The solar cell parameters computed within the SQ limit suggest that as the NW diameter increase, the respective current density of the NWs show markable

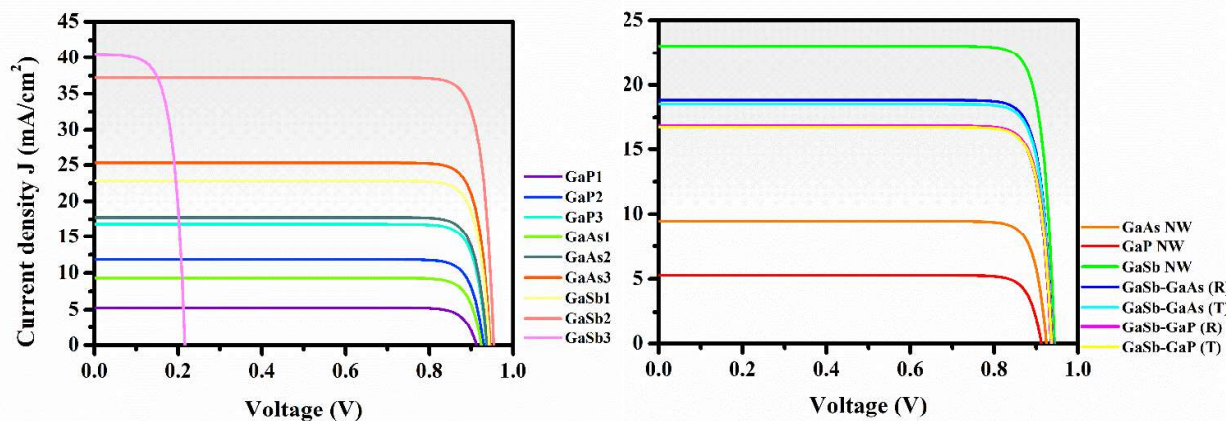


Figure 4.9. Computed JV curve for GaX (X=P, As, Sb) NWs and GaSb-GaX (X=As, P) HSNWs with comparison to the pristine GaP, GaAs and GaSb NWs.

enhancement, but the difference in the open-circuit voltage is negligible, except for the case of GaSb NW with  $\sim 3$  nm diameter. This is because of the lower electronic band gap of the NW ( $< 1$  eV) as compared to other systems. This results in the enhancement in the power conversion efficiency of the systems. The increase in diameter also causes enhancement in the overall efficiency of the systems with highest efficiency of 31% observed for GaSb NW with  $\sim 2$  nm diameter. Moving towards the performance of HSNWs, we can clearly observe the effect of bandgap on the power conversion efficiency (see Table 4.3). As the SQ limited parameters are bandgap dependent, we can observe negligible difference in the power conversion efficiency of the HSNWs with different core NWs. Moreover, due to the admirable moderate bandgap, the GaSb-GaAs HSNWs possess higher efficiency than the GaSb-GaP HSNWs. The current density ( $J$ ) as a function of potential ( $V$ ) generated is presented in Figure 4.9. The figure clearly reveals that the area under the curve of JV curve is highest in case of GaSb2 NW which agrees well with the computed power conversion efficiency. On the other hand, the area under the curve for the HSNWs with distinct core shape overlap with each other due to similarity in electronic bandgap. This observation

validates the direct dependence of SQ limited efficiency with the electronic band gap. Although, the SQ limit accounts for the highest theoretically possible power conversion efficiency, and the absorption spectra dependent performance can be obtained under the spectroscopic limited maximum efficiency (SMLE) approach.

### **4.3 Conclusion**

The DFT based *state-of-art* computations on GaSb-GaX (X=As, P) core/shell based HSNWs were performed to investigate the ground state structural, electronic and optical transport properties. The GaX (X=P, As, Sb) compounds being unique in III-V group were selected to understand the quantum confinement, size, shape and composition dependent properties and to test respective field of application. The low lattice mismatch and admissible range of cohesion (that is quite higher than the respective pristine NWs) validate energetically stable structures and indicate possibility of construction of proposed radial HSNW. Spatially aligned electronic edge states of all four HSNWs unravel that the nature of the heterointerface is of type-II which is most desirable for optoelectronic, photovoltaic and photocatalytic applications. Furthermore, the electronic bandgap of all four HSNWs is found to be within the range of optical regime of electro-magnetic spectrum, with GaSb-GaP (R) HSNW with direct electronic bandgap. Also, the low band offset between the edge states of the hetero NWs (see Fig. 4.6) is indicative of fast and adaptive carrier transport through the hetero-interface. These key features of the HSNWs showcase all desired properties that an ideal heterostructure should possess for cutting-edge energy applications. At last, to get overview of the optical transport through the HSNWs, the complex di-electric function as a function of photon energy was

computed, which suggests that the absorption of the HSNWs occurs within and at beyond optical regime. This implicates the applicability of the HSNWs within the optical and UV regime. Inspired from the electro-optic properties of the systems, the solar cell parameters for the GaX NWs and the GaSb-GaX HSNWs were computed. The results indicate the GaSb NW with  $\sim 2$  nm diameter possesses highest power conversion efficiency of 31% amongst the considered systems, and under heterostructured configuration, the GaSb-GaAs HSNWs possess higher efficiency ( $\sim 18\%$ ) than the GaSb-GaP HSNWs. The SQ limited solar power conversion efficiency of the systems are impressive and depict bandgap and geometry dependent response. It is foreseen that the present foundational study on GaX based HSNWs paves a path towards multi-shaped HSNWs for tuning the electro-optic transport via formation of type-II interface which is of immense importance in case of photovoltaic devices.

## References

- (1) Filho, A. G. S.; Fagan, S. B. Nanomaterials Properties. In *Nanostructured Materials for Engineering Applications*; Springer Berlin Heidelberg, 2011; pp 5–22. [https://doi.org/10.1007/978-3-642-19131-2\\_2](https://doi.org/10.1007/978-3-642-19131-2_2).
- (2) Wu, Z.; Neaton, J. B.; Grossman, J. C. Quantum Confinement and Electronic Properties of Tapered Silicon Nanowires. *Phys. Rev. Lett.* **2008**, *100* (24), 236805. <https://doi.org/10.1103/PhysRevLett.100.246804>.
- (3) Liang, Y.; Zhai, L.; Zhao, X.; Xu, D. Band-Gap Engineering of Semiconductor Nanowires through Composition Modulation. *J. Phys. Chem. B* **2005**, *109* (15), 7120–7123. <https://doi.org/10.1021/jp045566e>.
- (4) dos Santos, C. L.; Piquini, P.; Magri, R. Band Folding, Strain, Confinement, and Surface Relaxation Effects on the Electronic Structure of GaAs and GaP: From Bulk to Nanowires. *Eur. Phys. J. B* **2019**, *92* (9). <https://doi.org/10.1140/epjb/e2019-100288-y>.
- (5) Hoch, L. B.; Szymanski, P.; Ghuman, K. K.; Hea, L.; Liao, K.; Qiao, Q.; Reyes, L. M.; Zhu, Y.; El-Sayed, M. A.; Singh, C. V.; et al. Carrier Dynamics and the Role of Surface Defects: Designing a Photocatalyst for Gas-Phase CO<sub>2</sub> Reduction. *Proc. Natl. Acad. Sci. U. S. A.* **2016**, *113* (50), E8011–E8020. <https://doi.org/10.1073/pnas.1609374113>.

- (6) Layek, A.; Manna, B.; Chowdhury, A. Carrier Recombination Dynamics through Defect States of ZnO Nanocrystals: From Nanoparticles to Nanorods. *Chem. Phys. Lett.* **2012**, *539–540*, 133–138. <https://doi.org/10.1016/j.cplett.2012.05.028>.
- (7) Borg, B. M.; Dick, K. A.; Ganjipour, B.; Pistol, M. E.; Wernersson, L. E.; Thelander, C. InAs/GaSb Heterostructure Nanowires for Tunnel Field-Effect Transistors. *Nano Lett.* **2010**, *10* (10), 4080–4085. <https://doi.org/10.1021/nl102145h>.
- (8) Zhang, Y.; Wu, J.; Aagesen, M.; Liu, H. III-V Nanowires and Nanowire Optoelectronic Devices. *Journal of Physics D: Applied Physics*. 2015. <https://doi.org/10.1088/0022-3727/48/46/463001>.
- (9) Zhang, X.; Liu, B.; Liu, Q.; Yang, W.; Xiong, C.; Li, J.; Jiang, X. Ultrasensitive and Highly Selective Photodetections of UV-a Rays Based on Individual Bicrystalline GaN Nanowire. *ACS Appl. Mater. Interfaces* **2017**, *9* (3), 2669–2677. <https://doi.org/10.1021/acsami.6b14907>.
- (10) Wang, T.; Chai, Y.; Ma, D.; Chen, W.; Zheng, W.; Huang, S. Multidimensional CdS Nanowire/CdIn<sub>2</sub>S<sub>4</sub> Nanosheet Heterostructure for Photocatalytic and Photoelectrochemical Applications. *Nano Res.* **2017**, *10* (8), 2699–2711. <https://doi.org/10.1007/s12274-017-1473-y>.
- (11) Thelander, C.; Agarwal, P.; Brongersma, S.; Eymery, J.; Feiner, L. F.; Forchel, A.; Scheffler, M.; Riess, W.; Ohlsson, B. J.; Gösele, U.; et al. Nanowire-Based One-Dimensional Electronics. *Mater. Today* **2006**, *9* (10), 28–35. [https://doi.org/10.1016/S1369-7021\(06\)71651-0](https://doi.org/10.1016/S1369-7021(06)71651-0).
- (12) Roger, I.; Shipman, M. A.; Symes, M. D. Earth-Abundant Catalysts for Electrochemical and Photoelectrochemical Water Splitting. *Nature Reviews Chemistry*. 2017. <https://doi.org/10.1038/s41570-016-0003>.
- (13) Yang, L.; Motohisa, J.; Fukui, T.; Jia, L. X.; Zhang, L.; Geng, M. M.; Chen, P.; Liu, Y. L.; Wang, T. Fabry-Pérot Microcavity Modes Observed in the Micro-Photoluminescence Spectra of the Single Nanowire with InGaAs/GaAs Heterostructure. *Opt. Express* **2009**, *17* (11), 9337. <https://doi.org/10.1364/oe.17.009337>.
- (14) Qian, F.; Li, Y.; Gradečak, S.; Park, H. G.; Dong, Y.; Ding, Y.; Wang, Z. L.; Lieber, C. M. Multi-Quantum-Well Nanowire Heterostructures for Wavelength-Controlled Lasers. *Nat. Mater.* **2008**, *7* (9), 701–706. <https://doi.org/10.1038/nmat2253>.
- (15) Yan, X.; Zhang, X.; Li, J.; Wu, Y.; Cui, J.; Ren, X. Fabrication and Optical Properties of GaAs/InGaAs/GaAs Nanowire Core-Multishell Quantum Well Heterostructures. *Nanoscale* **2015**, *7* (3), 1110–1115. <https://doi.org/10.1039/c4nr05486e>.
- (16) Yan, X.; Fan, S.; Zhang, X.; Ren, X. Analysis of Critical Dimensions for Nanowire Core-Multishell Heterostructures. *Nanoscale Res. Lett.* **2015**, *10* (1), 1–7. <https://doi.org/10.1186/s11671-015-1097-7>.
- (17) Parkinson, P.; Joyce, H. J.; Gao, Q.; Tan, H. H.; Zhang, X.; Zou, J.; Jagadish, C.; Herz, L. M.; Johnston, M. B. Carrier Lifetime and Mobility Enhancement in Nearly Defect-

- Free Core-Shell Nanowires Measured Using Time-Resolved Terahertz Spectroscopy. *Nano Lett.* **2009**, *9* (9), 3349–3353. <https://doi.org/10.1021/nl9016336>.
- (18) Joyce, H. J.; Wong-Leung, J.; Yong, C. K.; Docherty, C. J.; Paiman, S.; Gao, Q.; Tan, H. H.; Jagadish, C.; Lloyd-Hughes, J.; Herz, L. M.; et al. Ultralow Surface Recombination Velocity in InP Nanowires Probed by Terahertz Spectroscopy. *Nano Lett.* **2012**, *12* (10), 5325–5330. <https://doi.org/10.1021/nl3026828>.
- (19) Caroff, P.; Messing, M. E.; Mattias Borg, B.; Dick, K. A.; Deppert, K.; Wernersson, L. E. InSb Heterostructure Nanowires: MOVPE Growth under Extreme Lattice Mismatch. *Nanotechnology* **2009**, *20* (49), 495606. <https://doi.org/10.1088/0957-4484/20/49/495606>.
- (20) Kavanagh, K. L. Misfit Dislocations in Nanowire Heterostructures. *Semicond. Sci. Technol.* **2010**, *25* (2), 024006. <https://doi.org/10.1088/0268-1242/25/2/024006>.
- (21) Cirlin, G. E.; Dubrovskii, V. G.; Soshnikov, I. P.; Sibirev, N. V.; Samsonenko, Y. B.; Bouravleuv, A. D.; Harmand, J. C.; Glas, F. Critical Diameters and Temperature Domains for MBE Growth of III-V Nanowires on Lattice Mismatched Substrates. *Phys. Status Solidi - Rapid Res. Lett.* **2009**, *3* (4), 112–114. <https://doi.org/10.1002/pssr.200903057>.
- (22) Fröberg, L. E.; Wacaser, B. A.; Wagner, J. B.; Jeppesen, S.; Ohlsson, B. J.; Deppert, K.; Samuelson, L. Transients in the Formation of Nanowire Heterostructures. *Nano Lett.* **2008**, *8* (11), 3815–3818. <https://doi.org/10.1021/nl802149v>.
- (23) Himwas, C.; Collin, S.; Chen, H. L.; Patriarche, G.; Oehler, F.; Travers, L.; Saket, O.; Julien, F. H.; Harmand, J. C.; Tchernycheva, M. Correlated Optical and Structural Analyses of Individual GaAsP/GaP Core-Shell Nanowires. *Nanotechnology* **2019**, *30* (30), 304001. <https://doi.org/10.1088/1361-6528/ab1760>.
- (24) Johnson, J. C.; Knutsen, K. P.; Yan, H.; Law, M.; Zhang, Y.; Yang, P.; Saykally, R. J. Ultrafast Carrier Dynamics in Single ZnO Nanowire and Nanoribbon Lasers. *Nano Lett.* **2004**, *4* (2), 197–204. <https://doi.org/10.1021/nl034780w>.
- (25) Lo, S. S.; Major, T. A.; Petchsang, N.; Huang, L.; Kuno, M. K.; Hartland, G. V. Charge Carrier Trapping and Acoustic Phonon Modes in Single CdTe Nanowires. *ACS Nano* **2012**, *6* (6), 5274–5282. <https://doi.org/10.1021/nl3010526>.
- (26) Li, Y.; Qian, F.; Xiang, J.; Lieber, C. M. Nanowire Electronic and Optoelectronic Devices. *Mater. Today* **2006**, *9* (10), 18–27. [https://doi.org/10.1016/S1369-7021\(06\)71650-9](https://doi.org/10.1016/S1369-7021(06)71650-9).
- (27) Nolan, M.; O’Callaghan, S.; Fagas, G.; Greer, J. C.; Frauenheim, T. Silicon Nanowire Band Gap Modification. *Nano Lett.* **2007**, *7* (1), 34–38. <https://doi.org/10.1021/nl061888d>.
- (28) Tersoff, J. Stable Self-Catalyzed Growth of III-V Nanowires. *Nano Lett.* **2015**, *15* (10), 6609–6613. <https://doi.org/10.1021/acs.nanolett.5b02386>.
- (29) Meister, S.; Peng, H.; McIlwrath, K.; Jarausch, K.; Zhang, X. F.; Cui, Y. Synthesis and

- Characterization of Phase-Change Nanowires. *Nano Lett.* **2006**, *6* (7), 1514–1517. <https://doi.org/10.1021/nl061102b>.
- (30) Dick, K. A.; Thelander, C.; Samuelson, L.; Caroff, P. Crystal Phase Engineering in Single InAs Nanowires. *Nano Lett.* **2010**, *10* (9), 3494–3499. <https://doi.org/10.1021/nl101632a>.
- (31) Qian, F.; Li, Y.; Gradečak, S.; Wang, D.; Barrelet, C. J.; Lieber, C. M. Gallium Nitride-Based Nanowire Radial Heterostructures for Nanophotonics. *Nano Lett.* **2004**, *4* (10), 1975–1979. <https://doi.org/10.1021/nl0487774>.
- (32) Wu, Y.; Xiang, J.; Yang, C.; Lu, W.; Lieber, C. M. Single-Crystal Metallic Nanowires and Metal/Semiconductor Nanowire Heterostructures. *Nature* **2004**, *430* (6995), 61–65. <https://doi.org/10.1038/nature02674>.
- (33) Samuelson, L.; Thelander, C.; Björk, M. T.; Borgström, M.; Deppert, K.; Dick, K. A.; Hansen, A. E.; Mårtensson, T.; Panev, N.; Persson, A. I.; et al. Semiconductor Nanowires for OD and ID Physics and Applications. *Phys. E Low-Dimensional Syst. Nanostructures* **2004**, *25* (2-3 SPEC.ISS.), 313–318. <https://doi.org/10.1016/j.physe.2004.06.030>.
- (34) Joyce, H. J.; Gao, Q.; Tan, H. H.; Jagadish, C.; Kim, Y.; Fickenscher, M. A.; Perera, S.; Hoang, T. B.; Smith, L. M.; Jackson, H. E.; et al. Unexpected Benefits of Rapid Growth Rate for III–V Nanowires. *Nano Lett.* **2009**, *9* (2), 695–701. <https://doi.org/10.1021/nl803182c>.
- (35) Lim, S. K.; Brewster, M.; Qian, F.; Li, Y.; Lieber, C. M.; Gradečak, S. Direct Correlation between Structural and Optical Properties of III - V Nitride Nanowire Heterostructures with Nanoscale Resolution. *Nano Lett.* **2009**, *9* (11), 3940–3944. <https://doi.org/10.1021/nl9025743>.
- (36) Jiang, X.; Xiong, Q.; Nam, S.; Qian, F.; Li, Y.; Lieber, C. M. InAs/InP Radial Nanowire Heterostructures as High Electron Mobility Devices. *Nano Lett.* **2007**, *7* (10), 3214–3218. <https://doi.org/10.1021/nl072024a>.
- (37) Hu, Y.; Churchill, H. O. H.; Reilly, D. J.; Xiang, J.; Lieber, C. M.; Marcus, C. M. A Ge/Si Heterostructure Nanowire-Based Double Quantum Dot with Integrated Charge Sensor. *Nat. Nanotechnol.* **2007**, *2* (10), 622–625. <https://doi.org/10.1038/nnano.2007.302>.
- (38) Songmuang, R.; Katsaros, G.; Monroy, E.; Spathis, P.; Bougerol, C.; Mongillo, M.; De Franceschi, S. Quantum Transport in GaN/AlN Double-Barrier Heterostructure Nanowires. *Nano Lett.* **2010**, *10* (9), 3545–3550. <https://doi.org/10.1021/nl1017578>.
- (39) Xiang, J.; Lu, W.; Hu, Y.; Wu, Y.; Yan, H.; Lieber, C. M. Ge/Si Nanowire Heterostructures as High-Performance Field-Effect Transistors. *Nature* **2006**, *441* (7092), 489–493. <https://doi.org/10.1038/nature04796>.
- (40) Guo, W.; Zhang, M.; Bhattacharya, P.; Heo, J. Auger Recombination in III-Nitride Nanowires and Its Effect on Nanowire Light-Emitting Diode Characteristics. *Nano Lett.*

- 2011, 11 (4), 1434–1438. <https://doi.org/10.1021/nl103649d>.
- (41) Ghosh, P.; Huang, M. Effects of Strain on Various Properties and Applications on One-Dimensional Nano-/Microstructures. *Journal of Materials Science*. Springer June 2020, pp 7208–7225. <https://doi.org/10.1007/s10853-020-04500-1>.
- (42) Trammell, T. E.; Zhang, X.; Li, Y.; Chen, L. Q.; Dickey, E. C. Equilibrium Strain-Energy Analysis of Coherently Strained Core-Shell Nanowires. *J. Cryst. Growth* **2008**, 310 (12), 3084–3092. <https://doi.org/10.1016/j.jcrysgro.2008.02.037>.
- (43) Oksenberg, E.; Martí-Sánchez, S.; Popovitz-Biro, R.; Arbiol, J.; Joselevich, E. Surface-Guided Core-Shell ZnSe@ZnTe Nanowires as Radial p-n Heterojunctions with Photovoltaic Behavior. *ACS Nano* **2017**, 11 (6), 6155–6166. <https://doi.org/10.1021/acsnano.7b02199>.
- (44) Himwas, C.; Collin, S.; Rale, P.; Chauvin, N.; Patriarche, G.; Oehler, F.; Julien, F. H.; Travers, L.; Harmand, J. C.; Tchernycheva, M. In Situ Passivation of GaAsP Nanowires. *Nanotechnology* **2017**, 28 (49), 495707. <https://doi.org/10.1088/1361-6528/aa9533>.
- (45) Zhang, S.; Connie, A. T.; Laleyan, D. A.; Nguyen, H. P. T.; Wang, Q.; Song, J.; Shih, I.; Mi, Z. On the Carrier Injection Efficiency and Thermal Property of InGaN/GaN Axial Nanowire Light Emitting Diodes. *IEEE J. Quantum Electron.* **2014**, 50 (6), 483–490. <https://doi.org/10.1109/JQE.2014.2317732>.
- (46) Zhang, Y.; Aagesen, M.; Holm, J. V.; Jørgensen, H. I.; Wu, J.; Liu, H. Self-Catalyzed GaAsP Nanowires Grown on Silicon Substrates by Solid-Source Molecular Beam Epitaxy. *Nano Lett.* **2013**, 13 (8), 3897–3902. <https://doi.org/10.1021/nl401981u>.
- (47) Qian, F.; Gradečak, S.; Li, Y.; Wen, C. Y.; Lieber, C. M. Core/Multishell Nanowire Heterostructures as Multicolor, High-Efficiency Light-Emitting Diodes. *Nano Lett.* **2005**, 5 (11), 2287–2291. <https://doi.org/10.1021/nl051689e>.
- (48) Li, L.; Gu, L.; Lou, Z.; Fan, Z.; Shen, G. ZnO Quantum Dot Decorated Zn<sub>2</sub>SnO<sub>4</sub> Nanowire Heterojunction Photodetectors with Drastic Performance Enhancement and Flexible Ultraviolet Image Sensors. *ACS Nano* **2017**, 11 (4), 4067–4076. <https://doi.org/10.1021/acsnano.7b00749>.
- (49) Zheng, Z.; Gan, L.; Zhang, J. B.; Zhuge, F.; Zhai, T. Y. An Enhanced UV-Vis-NIR and Flexible Photodetector Based on Electrospun ZnO Nanowire Array/PbS Quantum Dots Film Heterostructure. *Adv. Sci.* **2017**, 4 (3). <https://doi.org/10.1002/advs.201600316>.
- (50) Plissard, S.; Dick, K. A.; Wallart, X.; Caroff, P. Gold-Free GaAs/GaAsSb Heterostructure Nanowires Grown on Silicon. *Appl. Phys. Lett.* **2010**, 96 (12). <https://doi.org/10.1063/1.3367746>.
- (51) Mourik, V.; Zuo, K.; Frolov, S. M.; Plissard, S. R.; Bakkers, E. P. A. M.; Kouwenhoven, L. P. Signatures of Majorana Fermions in Hybrid Superconductor-Semiconductor Nanowire Devices. *Science* (80-. ). **2012**, 336 (6084), 1003–1007. <https://doi.org/10.1126/science.1222360>.
- (52) Kohn, W.; Becke, A. D.; Parr, R. G. Density Functional Theory of Electronic Structure.

- J. Phys. Chem.* **1996**, *100* (31), 12974–12980. <https://doi.org/10.1021/jp9606691>.
- (53) Head, J. D.; Zerner, M. C. A Broyden-Fletcher-Goldfarb-Shanno Optimization Procedure for Molecular Geometries. *Chem. Phys. Lett.* **1985**, *122* (3), 264–270. [https://doi.org/10.1016/0009-2614\(85\)80574-1](https://doi.org/10.1016/0009-2614(85)80574-1).
- (54) Perdew, J. P.; Zunger, A. Self-Interaction Correction to Density-Functional Approximations for Many-Electron Systems. *Phys. Rev. B* **1981**, *23* (10), 5048–5079. <https://doi.org/10.1103/PhysRevB.23.5048>.
- (55) Kolmakov, A.; Klenov, D. O.; Lilach, Y.; Stemmer, S.; Moskovitst, M. Enhanced Gas Sensing by Individual SnO<sub>2</sub> Nanowires and Nanobelts Functionalized with Pd Catalyst Particles. *Nano Lett.* **2005**, *5* (4), 667–673. <https://doi.org/10.1021/nl050082v>.
- (56) Grimme, S.; Antony, J.; Ehrlich, S.; Krieg, H. A Consistent and Accurate Ab Initio Parametrization of Density Functional Dispersion Correction (DFT-D) for the 94 Elements H-Pu. *J. Chem. Phys.* **2010**, *132* (15). <https://doi.org/10.1063/1.3382344>.
- (57) Pack, J. D.; Monkhorst, H. J. “special Points for Brillouin-Zone Integrations”-a Reply. *Physical Review B*. American Physical Society August 1977, pp 1748–1749. <https://doi.org/10.1103/PhysRevB.16.1748>.
- (58) Marzari, N.; Vanderbilt, D.; De Vita, A.; Payne, M. C. Thermal Contraction and Disorder of the Al(110) Surface. *Phys. Rev. Lett.* **1999**, *82* (16), 3296–3299. <https://doi.org/10.1103/PhysRevLett.82.3296>.
- (59) Gajdoš, M.; Hummer, K.; Kresse, G.; Furthmüller, J.; Bechstedt, F. Linear Optical Properties in the Projector-Augmented Wave Methodology. *Phys. Rev. B - Condens. Matter Mater. Phys.* **2006**, *73* (4). <https://doi.org/10.1103/PhysRevB.73.045112>.
- (60) Harl, J.; Kresse, G.; Sun, L. D.; Hohage, M.; Zeppenfeld, P. Ab Initio Reflectance Difference Spectra of the Bare and Adsorbate Covered Cu(110) Surfaces. *Phys. Rev. B - Condens. Matter Mater. Phys.* **2007**, *76* (3). <https://doi.org/10.1103/PhysRevB.76.035436>.
- (61) Joshi, N.; Upadhyay, D.; Pandya, A.; Jha, P. K. Predicting the Stable Rhodium Based Chalcopyrites with Remarkable Optical Properties. *J. Appl. Phys.* **2019**, *126* (23), 235705. <https://doi.org/10.1063/1.5127010>.
- (62) Guo, M.; Xie, K.; Lin, J.; Yong, Z.; Yip, C. T.; Zhou, L.; Wang, Y.; Huang, H. Design and Coupling of Multifunctional TiO<sub>2</sub> Nanotube Photonic Crystal to Nanocrystalline Titania Layer as Semi-Transparent Photoanode for Dye-Sensitized Solar Cell. *Energy Environ. Sci.* **2012**, *5* (12), 9881–9888. <https://doi.org/10.1039/c2ee22854h>.
- (63) Som, N. N.; Sharma, V.; Mankad, V.; Attygalle, M. L. C.; Jha, P. K. Role of CuAlO<sub>2</sub> as an Absorber Layer for Solar Energy Converter. *Sol. Energy* **2019**, *193* (September), 799–805. <https://doi.org/10.1016/j.solener.2019.09.098>.
- (64) Gajaria, T. K.; Dabhi, S. D.; Jha, P. K. Ab Initio Energetics and Thermoelectric Profiles of Gallium Pnictide Polytypes. *Sci. Rep.* **2019**, *9* (1). <https://doi.org/10.1038/s41598-019-41982-9>.